The Astrophysical Journal, 925:170 (9pp), 2022 February 1 https://doi.org/10.3847/1538-4357/ac4096

Causal Interaction between the Subsurface Rotation Rate Residuals and Radial Magnetic Field in Different Timescales

Fadil Inceoglu[1], Rachel Howe[2,3], and Paul T. M. Loto'aniu[4,5]
[1] GFZ German Research Centre for Geosciences, Telegrafenberg, D-14473, Potsdam, Germany; fadil@gfz-potsdam.de
[2] School of Physics and Astronomy, University of Birmingham, Edgbaston, Birmingham, B15 2TT, UK
[3] Stellar Astrophysics Centre (SAC), Department of Physics and Astronomy, Aarhus University, Ny Munkegade 120, DK-8000 Aarhus C, Denmark
[4] Cooperative Institute for Research in Environmental Sciences, University of Colorado Boulder, Boulder, CO 80309, USA
[5] National Centers for Environmental Information, National Oceanographic and Atmospheric Administration, Boulder, CO, USA
Received 2021 November 7; revised 2021 December 2; accepted 2021 December 5; published 2022 February 3

Abstract

We studied the presence and spatiotemporal characteristics and evolution of the variations in the differential rotation rates and radial magnetic fields in the Schwabe and quasi-biennial-oscillation (QBO) timescales. To achieve these objectives, we used rotation rate residuals and radial magnetic field data from the Michelson Doppler Imager on the Solar and Heliospheric Observatory and the Helioseismic and Magnetic Imager on the Solar Dynamics Observatory, extending from 1996 May to 2020 August, covering solar cycles 23 and 24, respectively. Under the assumption that the radial surface magnetic field is nonlocal and the differential rotation is symmetric around the equator, our results suggest that the source region of the Schwabe cycle is confined between ∼30° N and S throughout the convection zone. As for the source region of the QBO, our results suggest that it is below 0.78 $R_{\odot}$.

Unified Astronomy Thesaurus concepts: The Sun (1693); Solar rotation (1524); Solar magnetic fields (1503); Solar interior (1500)

1. Introduction

The Sun is a magnetically active variable star. The Sun governs the space-climate and space-weather throughout the heliosphere via its magnetic activity variations in short-, mid-, and long-term timescales. The most well-known magnetic activity cycle is the Schwabe cycle (Schwabe 1844), the period of which ranges from 9 to 13 yr. The Schwabe cycle is superimposed on longer-term variations, such as ∼90 yr Gleissberg (Gleissberg 1939) and ∼210 yr Suess (Suess 1980) cycles. The Sun also shows shorter quasiperiodic variations that are 160 day Rieger-type periodicities (Rieger et al. 1984) and quasi-biennial oscillations (QBOs), the period of which ranges from 0.6 to 4 yr. It was also pointed out that there is a clear separation at 1.5 yr, indicating two groups of variations below and above this value (Bazilevskaya et al. 2014).

The QBOs are shown to be more intermittent signals, and the variations in their amplitude are in-phase with the Schwabe cycle, meaning they attain their highest (lowest) amplitude during the solar cycle maxima (minima; Bazilevskaya et al. 2014). Together with exhibiting signals over all solar latitudes (Vecchio et al. 2012), they are also shown to behave differently in each solar hemisphere (Gurgenashvili et al. 2017; Inceoglu et al. 2019). The QBOs are found to be present from the subsurface layers to the surface of the Sun, and they can even be identified in the neutron counting rates measured on Earth as indicators of the Galactic cosmic-ray intensities (Benevolenskaya 1998; Kudela et al. 2010; Simoniello et al. 2012; Vecchio et al. 2012). Recently, Inceoglu et al. (2021) showed that the rotation rate residuals also show QBOs, and their amplitude increases with increasing depth. Therefore, the QBOs are thought to be global phenomena extending from the subsurface layers of the Sun to the Earth.

Among the physical mechanisms that were proposed to explain the existence and spatiotemporal behaviors of the QBOs, we can include spatiotemporal fragmentation of radial profiles of the rotation rates (Simoniello et al. 2013), 180° shifting of the active longitudes (Berdyugina & Usoskin 2003), a secondary dynamo operating in the subsurface shear layer at 0.95 $R_{\odot}$ (Benevolenskaya 1998), instability of the magnetic Rossby waves in the tachocline (Zaqarashvili et al. 2010), and tachocline nonlinear oscillations (TNOs) through periodic energy exchange between the Rossby waves, differential rotation, and the present toroidal field (Dikpati et al. 2018). In addition, based on results from a fully nonlinear flux transport dynamo, Inceoglu et al. (2019) proposed that there are indications for the QBOs to be generated via interplay between the flow and magnetic fields, where the turbulent α-mechanism works in the lower half of the solar convection zone, which extends from 0.70 $R_{\odot}$ to the surface. The bottom of the convection zone overlaps with the region of strong radial shear. Above this region, a differential rotation pattern that depends strongly on latitude takes place (Howe 2009).

Are the interactions between the magnetic and flow fields, as investigated by rotation rate residuals and radial magnetic fields, in the Schwabe and QBO timescales different at different depths and latitudes? Are there any preferred locations for the generation of these cyclic variations in the Sun's magnetic activity levels? To answer these questions, we utilized lagged–cross-correlation and convergent cross mapping (CCM) analyses using surface magnetic field and subsurface flow field data from the Michelson Doppler Imager (MDI) on the Solar and Heliospheric Observatory (SOHO) and the Helioseismic and Magnetic Imager (HMI) on the Solar Dynamics Observatory (SDO), covering solar cycles 23 and 24.

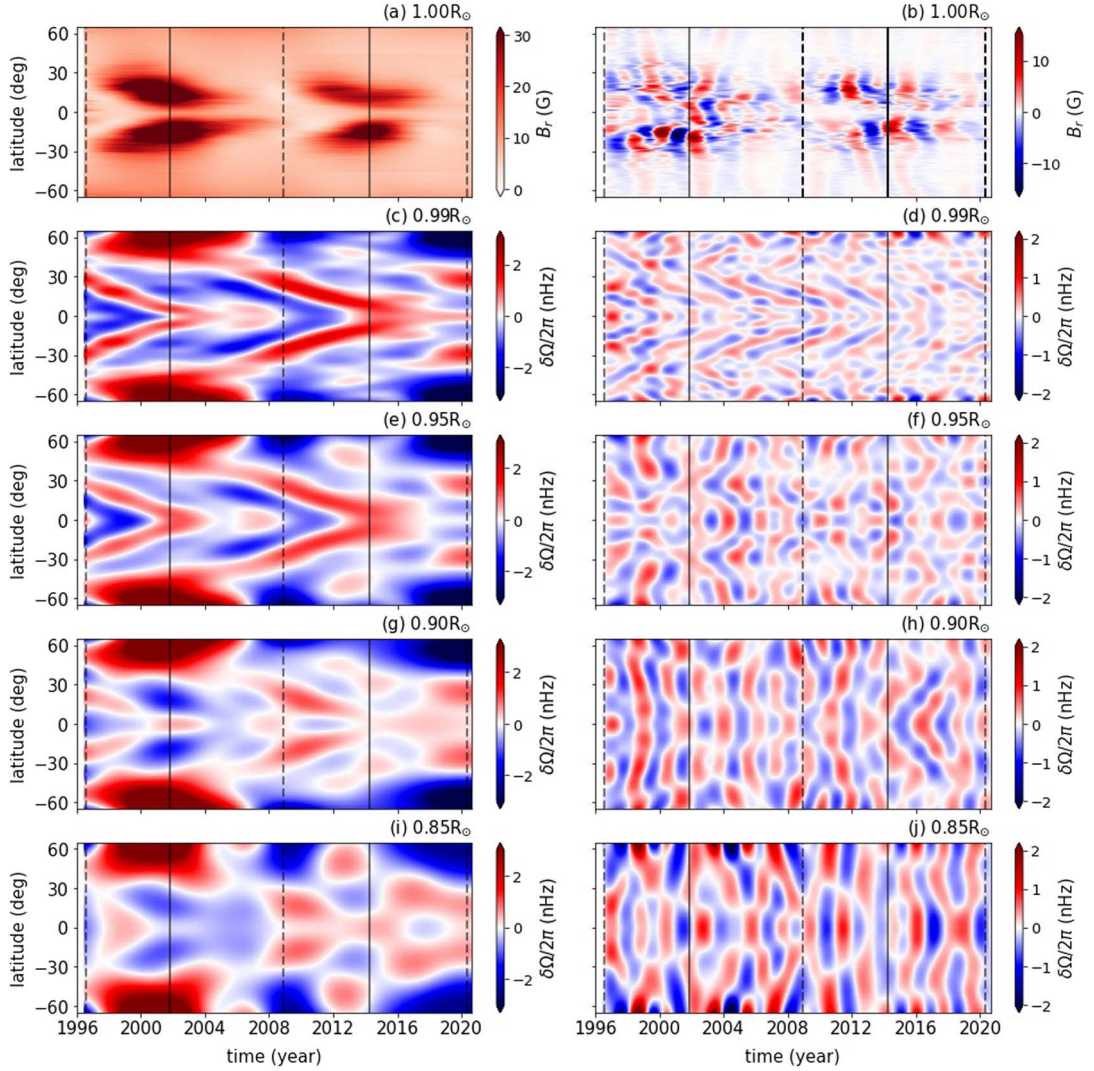

Figure 1. The left panels (a), (c), (e), (g), and (i) show low-pass filtered average absolute magnetic field strength and rotation rate residuals covering solar cycles 23 and 24. The right panels (b), (d), (f), (h), and (j) display the bandpass filtered average absolute magnetic field and rotation rate residuals covering solar cycles 23 and 24. Note that the limit of the color bar in Figure 1(b) shows fluctuations around the mean and not signed magnetic field strength. Vertical dashed lines show solar cycle minima, while the vertical solid lines show solar cycle maxima. Also note that the rotation rate residuals are flipped around the equator.

2. Data

We calculated the rotation rates based on regularized least-squares (RLS) code using frequencies derived from MDI/SOHO and HMI/SDO data. The rotation rates between 1996 May and 2011 February are calculated based on 59 sets of rotational splittings from 72 day spectra of MDI observations, while for the period between 2010 May to 2020 August, they were based on 53 sets from HMI. To splice the two data sets, we calculated an offset using the mean difference between the HMI and MDI rotation profiles over the five periods, where they overlap. This offset was applied because data from the MDI might be influenced by some systematic effects, which do not influence data from the HMI (Howe et al. 2013).

The surface magnetic field data for the period spanning from Carrington Rotation (CR) 1909 (1996 May) to 2104 (2010 December) are calculated using MDI radial magnetic field synoptic charts (Scherrer et al. 1995), while for the period from CR 2097 (2010 June) to CR 2235 (2020 October), we used HMI's radial magnetic field synoptic charts (Scherrer et al. 2012). First of all we converted signed magnetic field strengths into unsigned magnetic field strength by simply taking the absolute values in each synoptic map per CR and then averaged them in time per latitude. To merge the two data sets, we re-scaled the HMI data using relationships given in Liu et al. (2012).

Following that, to obtain the same temporal and spatial resolution, we interpolated the merged rotation rate residual data using the cubic spline method in 2D.

3. Analyses and Results

To study whether there are differences in interactions between the magnetic and flow fields in the Schwabe and the QBO timescales at different depths of the Sun, we merged the MDI/SOHO and HMI/SDO synoptic maps for radial magnetic fields spanning the last two solar cycles. In addition, we calculated the rotation rate residuals based on RLS code using frequencies derived from MDI and HMI data. Furthermore, to remove the potential effects from the annual periodic variations caused by the Earth's orbital inclination and tilt of the solar rotation axis, we low-pass filtered the data with a cutoff

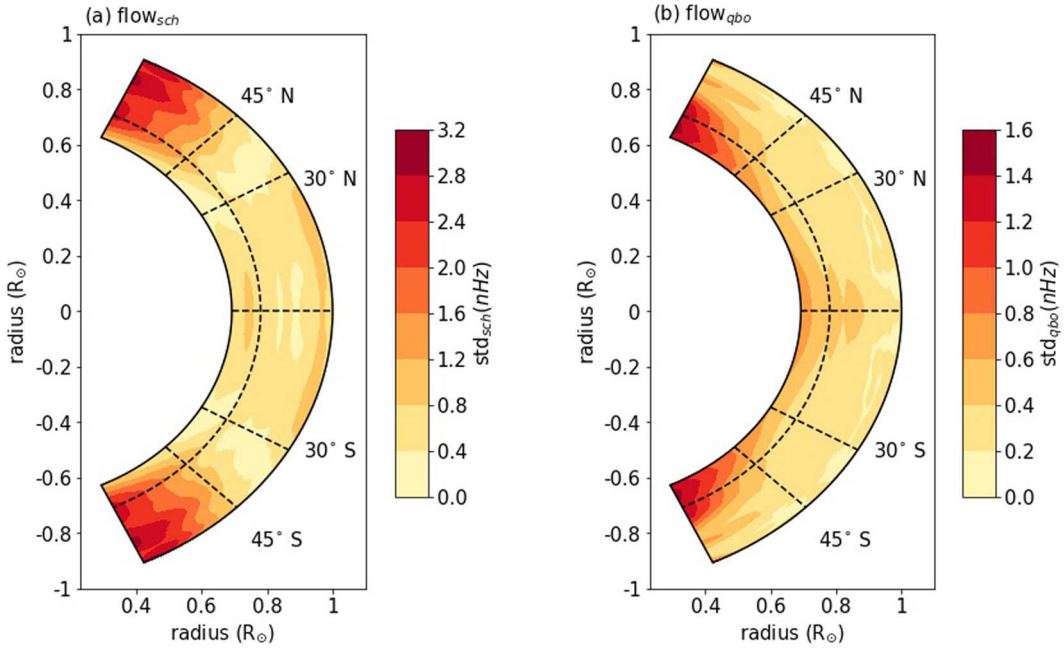

Figure 2. Amplitude of variations in the rotation rate residuals as a function of depth and latitude for the Schwabe timescale (a) and the QBO timescale (b). The dashed lines show 0.78 $R_\odot$.

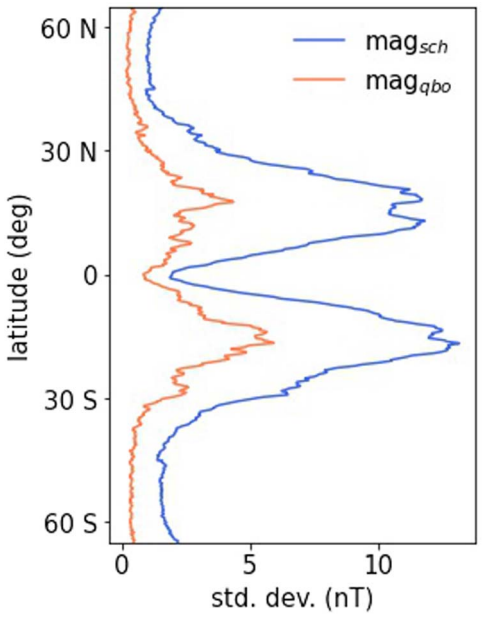

Figure 3. Amplitude of variations in the radial magnetic field as a function of latitude for the Schwabe timescale (blue) and the QBO timescale (orange).

frequency of 1.5 yr^{-1} using a Butterworth filter of degree 5. The Butterworth filter is a maximally flat filter in the passband that avoids any distortion of the low-frequency components of the signal. They can also be used as low-pass, high-pass, and bandpass filters (Roberts & Roberts 1978).

The Schwabe cycle and QBOs have periods spanning between 9–13 yr and 1.5–4 yr, respectively. Therefore, to separate the average unsigned magnetic field strengths and rotation rate residuals into two different timescales, we used, once more, a Butterworth filter of degree 5 with a cutoff frequency of 4.5 yr^{-1}. The Butterworth filter has been applied to each depth under consideration for the rotation rate residuals extending from ∼0.70 $R_\odot$ to 1.00 $R_\odot$ and to the surface average unsigned magnetic field strengths. We limited the latitudinal interval between 65° N and S because of data gaps in the surface magnetic field data due to the tilt of the rotation axis of the Sun as well as progressively decreasing reliability of the inversion with increasing latitude (Howe 2009). We must note that the global helioseismic inversions cannot resolve the solar hemispheres; therefore, the values are flipped around the equator for convenience.

In the low-pass filtered data, variations in the average unsigned magnetic field strengths in the Schwabe timescale can clearly be observed, where the magnetic field is stronger in solar cycle 23 than that in solar cycle 24 (Figure 1(a)). We also show variations in the rotation rate residuals in the Schwabe timescale for selected solar depths of 0.99 $R_\odot$, 0.95 $R_\odot$, 0.90 $R_\odot$, and 0.85 $R_\odot$ in Figures 1(c), (e), (g), and (i), respectively. The rotation rate residuals in this timescale show faster-than-average and slower-than-average flow bands in each depth. There are pronounced differences in flow patterns in high latitudes above ∼45° between solar cycle 23 and 24. For example, at the solar cycle 23 maximum, there is a strong faster-than-average flow band above ∼45° latitude, whereas there is nothing similar at the solar cycle 24 maximum. During the declining phase of solar cycle 24, a slower-than-average flow band forms in the high latitudes, which cannot be observed during the same phase of solar cycle 23 (Figures 1(c), (e), (g), and (i)). The lower latitudes below ∼45° latitude, on the other hand, show very similar behavior, having slower-than-average and faster-than-average flow bands form close to ∼45° latitude and propagate equatorward throughout the solar cycles.

In the QBO timescale, the average unsigned magnetic field shows fluctuations around the mean value, which is generally confined between ∼35° N and S around the solar equator (Figure 1(b)). The rotation rate residuals in this timescale also show similar slower-than-average and faster-than-average flow bands distributed all latitudes throughout the solar cycles at each depth, except for those in 0.99 $R_\odot$, which show more

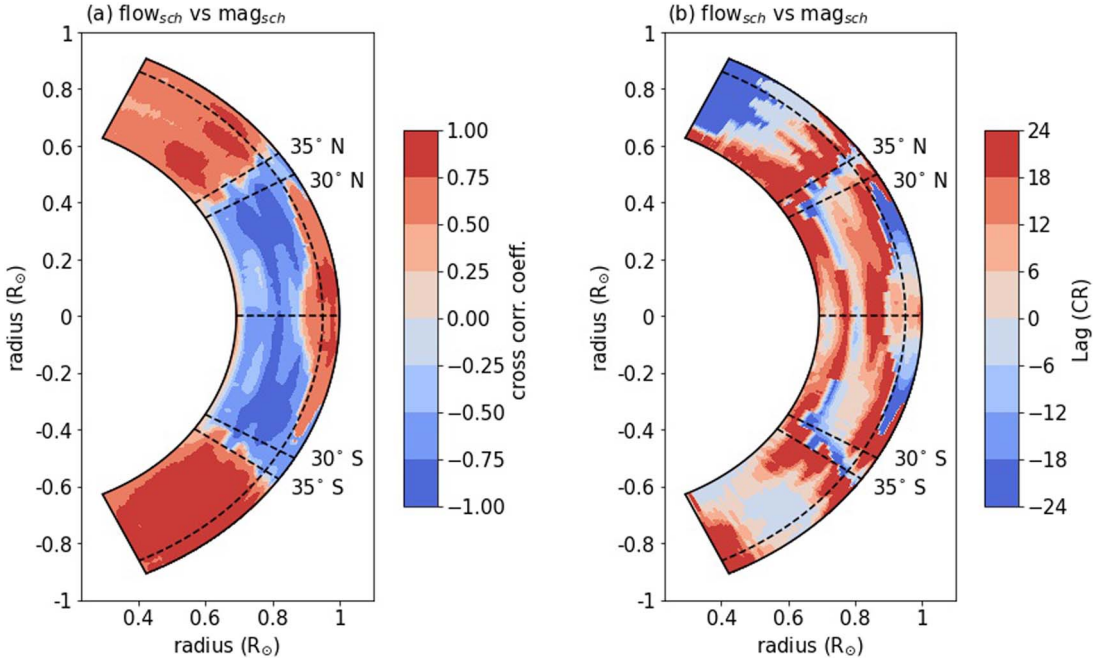

Figure 4. The highest lagged–cross-correlation coefficients (a) and the corresponding lags (b) between the rotation rate residuals (flow) and radial magnetic field (mag) in the Schwabe timescale. Note that the lag is denoted in Carrington Rotations (CR), and positive values indicate the magnetic field leading the flow field, while negative lag means the flow field is leading the magnetic field. The dashed lines show 0.95 $R_\odot$ to aid the eye (see the text).

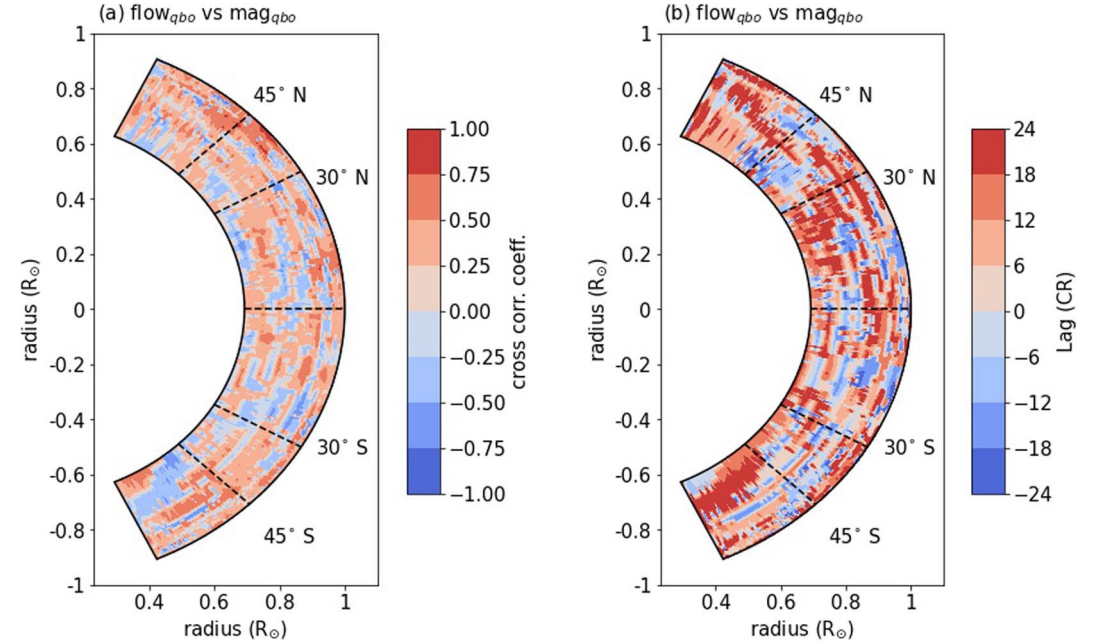

Figure 5. The same as Figure 4 but for the QBO timescale.

confined flow bands propagating equator-ward (Figures 1(d), (f), (h), and (j)).

3.1. Amplitude Variations in the Schwabe and QBO Timescales

We then calculate the amplitudes of the variations in the Schwabe and QBO timescales by simply calculating the standard deviations of variations at each latitude and depth ranging from 0.70 $R_\odot$ and 1.00 $R_\odot$ (Figures 2(a), and (b)). The amplitude of variations in the Schwabe timescale increases with increasing latitude after ∼35°, and it reaches its maximum around ∼60° latitude. The amplitude of variations in these higher latitudes shows similar values down to around 0.78 $R_\odot$, after which the amplitude becomes weaker. For the region between 0°–∼35° latitude, the amplitude of the variations shows a decreasing trend down to around 0.80 $R_\odot$, and it slightly increases (Figure 2(a)).

On the contrary, the amplitude of variations in the QBO timescales almost shows a reversed pattern. Although the latitudinal dependence of the amplitudes above ∼35° latitude is

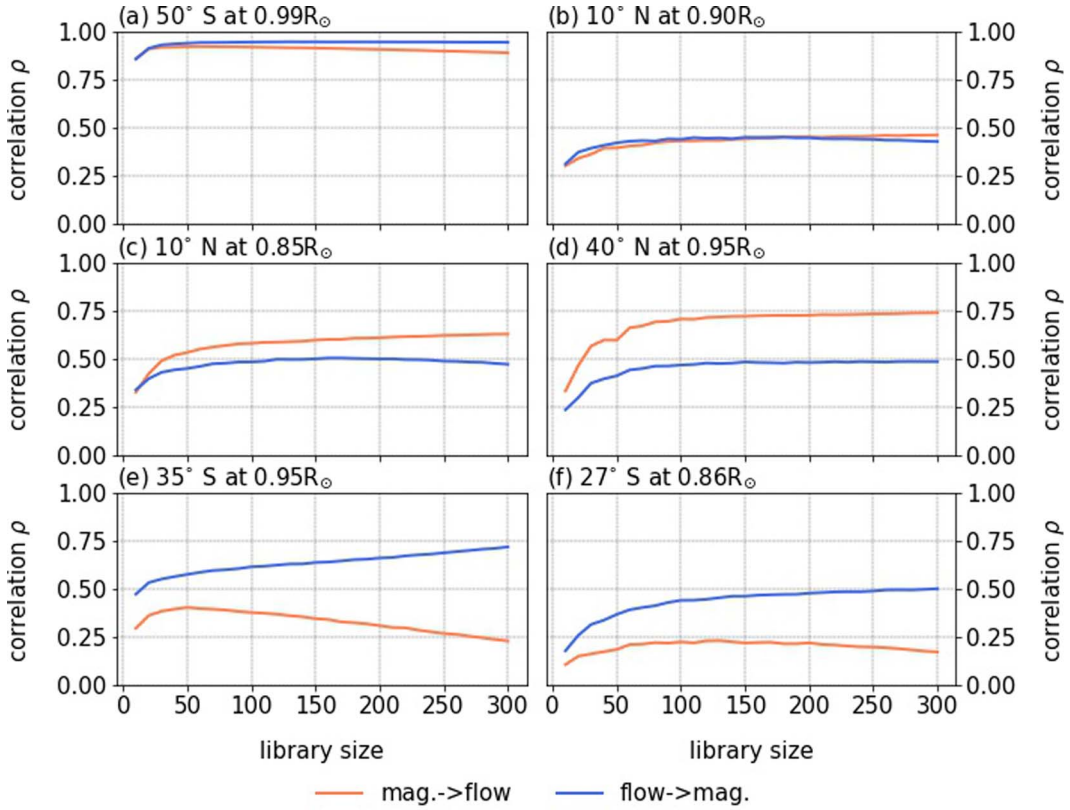

Figure 6. The direction of the causal interaction between the rotation rate residuals and radial magnetic field for the Schwabe (the left panel) and the QBO timescales (the right panel) for selected radius and latitudes. We give examples of where the directional causal influence cannot be determined (top panel), where there is a stronger magnetic field influence on the flow field (middle panel), and stronger flow field influence on the magnetic field (bottom panel) cases.

similar to those observed in the Schwabe timescale, the amplitude of variations reaches its maximum below 0.78 $R_\odot$. Below ∼35° latitude, on the other hand, the amplitude of variations increases with increasing depth, which is more pronounced around the solar equator (Figure 2(b)).

Similar to the ration rate residuals, we also calculated the amplitudes of variations in the unsigned magnetic field strengths at each latitude for the Schwabe and QBO timescales (Figure 3). The two timescales show almost identical amplitude variations as a function of latitude; the amplitudes are higher in the magnetic activity bands that are confined between latitudes ∼40° N and S, with maximum amplitudes observed around ∼15° N and S latitude. Interestingly, the amplitudes of variations in the Schwabe and QBO timescales decrease when we approach the solar equator from ∼15° N and S latitude (Figure 3).

To investigate the interaction between the flow and magnetic fields, we had to make two assumptions for further analyses: (i) the rotation profiles are symmetric around the equator, and (ii) the magnetic field measured on the surface is nonlocal in the convection zone, down to 0.71 $R_\odot$, as information on the magnetic field strengths below the surface of the Sun is not yet available. Earlier, it was shown that there are some asymmetries in the flow fields during the declining phase of cycle 23 and rising phase of solar cycle 24 at ∼0.99 $R_\odot$ (Lekshmi et al. 2018). Therefore, the results drawn from the following analyses must be approached with caution. The main idea here is to draw an average picture of the interactions between the magnetic and flow fields.

3.2. Lagged–Cross Correlations in the Schwabe and QBO Timescales

To investigate the linear relationship between the rotation rate residuals and average unsigned magnetic field, we use lagged–cross correlations at each depth and latitude.

In the Schwabe timescale, there is a strong positive correlation in almost all depths at latitudes above ∼35° (Figure 4(a)). In both solar hemispheres, the magnetic field is leading the flow field by 24 CRs at all depths in the latitudes between ∼35° and ∼45°. After around ∼45° up to ∼60° latitude, although there is still a positive correlation between the magnetic and flow fields, the flow field starts to lead the magnetic field with around six CRs. Above ∼60° latitude, the magnetic field leads the flow field in the southern solar hemisphere, while contrarily, the flow field leads the magnetic field in the northern hemisphere (Figure 4). Between ∼30° N and S around the solar equator and down to 0.95 $R_\odot$, there is a high positive correlation between the magnetic and flow fields, where the flow field leads the magnetic field with longer time with increasing latitude. However, between ∼5° N and S around the solar equator, the magnetic field is still leading the flow field. Between ∼30° and ∼35° latitude in the north and south, there is a strong inverse relationship between the radial magnetic field and rotation rate residuals at all depths, and the flow field is leading the magnetic field (Figure 4). At depths below 0.95 $R_\odot$ down to 0.71 $R_\odot$, there is an inverse relationship between the flow and magnetic fields. This region also exhibits that most of the time, the magnetic field is leading the flow field (Figure 4).

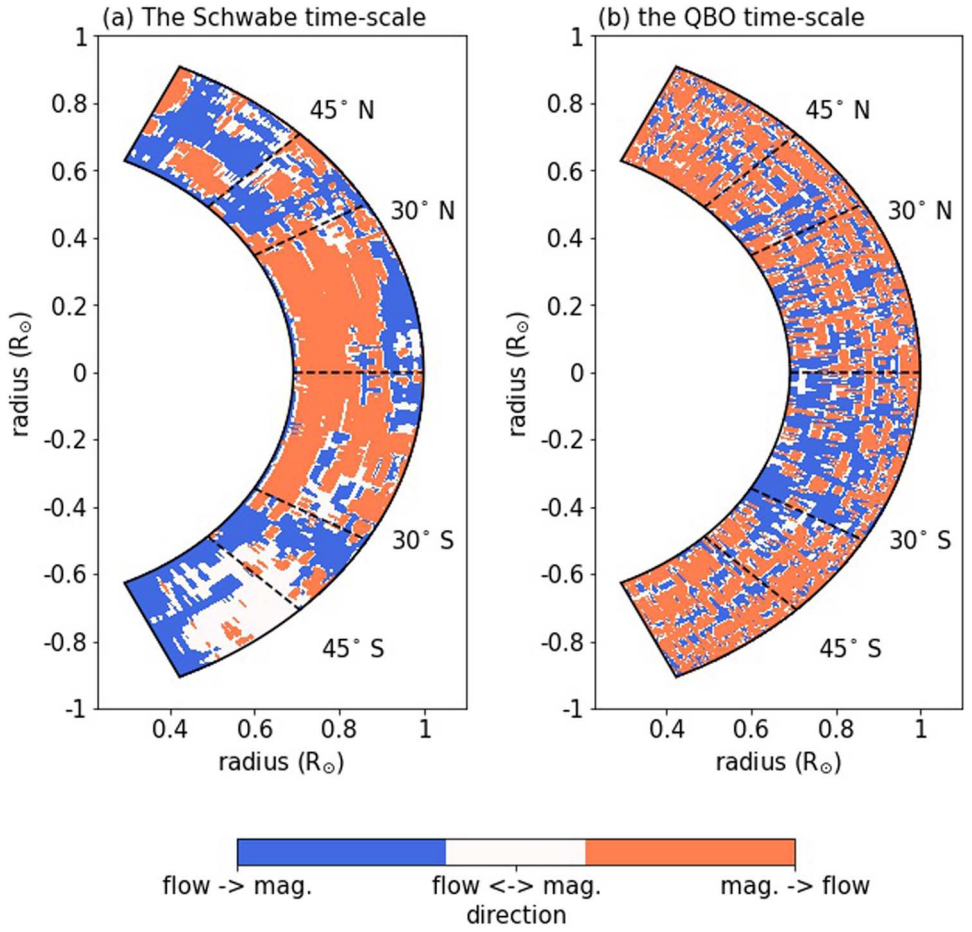

Figure 7. The direction of the causal interaction between the rotation rate residuals and radial magnetic field for the Schwabe (a) and the QBO timescales (b).

In the QBO timescale, on the contrary, there is not a clear pattern in the relationship between the rotation rate residuals and radial magnetic field (Figure 5). Some of the most pronounced features that are not present in the Schwabe timescale are the patches of marginally strong positive correlations through the convection zone, down to 0.71 $R_{\odot}$. These patches are observed to form in layers of positive and negative correlations. The magnetic field tends to lead the flow fields where the correlation coefficients are positive, while the flow field leads the magnetic field where the correlation is negative (Figure 5).

3.3. Causal Relationship in the Schwabe and QBO Timescales

To study the nonlinear causal relationship between the rotation rate residuals and average unsigned radial magnetic field, we used the CCM method, which was first introduced by Sugihara et al. (2012). CCM is a novel method that can detect if two time series originate from the same dynamical system based on measuring the predictability of one variable using the other (Sugihara et al. 2012). The same dynamical system acts as a common attractor manifold leading to the two time series to be causally linked. This case allows us to estimate the states of a causal variable using the affected variable. The overall predictive skill improves and converges with increasing time-series length. The key property that enables us to distinguish causation from simple correlation is this convergence criterion (Sugihara et al. 2012). In this study, we use the *pyEDM*[6] python library to study the cause and effect relationship between the rotation rate residuals and radial unsigned magnetic field strengths as well as bidirectional influences between the two variables in each latitude and radius (Sugihara et al. 2012; Ye & Sugihara 2016). To investigate the causal influence between the two variables, we first standardized each data set using their individual mean and standard deviation values, and then calculated their CCMs.

To give an example of the analysis, we first show three different results for each timescale (Figure 6). These results are for (i) where the causal influence of the magnetic field on the flow field is stronger (orange), (ii) where the causal influence of the flow field on the magnetic field is stronger (blue), and (iii) where the direction of the causal influence cannot be determined (white; Figure 6). CCM results for the Schwabe and the QBO timescales show that the causal relationship between the flow and the magnetic field is bidirectional at every depth and latitude, which is expected considering back-reaction of the Lorentz Force on the flow field. However, the degree of these causal influences at each depth and latitude varies. For example, at 50° S and at 0.99 $R_{\odot}$ in the Schwabe timescale and at 10° N and at 0.90 $R_{\odot}$ in the QBO timescale, the causal influence between the flow and magnetic fields is bidirectional with similar degrees (Figure 6(a) and b), whereas the causal influence of the magnetic field on the flow field is stronger at 10° N and at 0.85 $R_{\odot}$ and at 40° N and at 0.95 $R_{\odot}$ in the Schwabe and the QBO timescales, respectively (Figures 6(c) and (d)). On the

[6] URL: https://github.com/SugiharaLab/pyEDM.

other hand, the causal influence of the flow field on the magnetic field is stronger at 35° S latitude and at 0.95 $R_\odot$ in the Schwabe timescale and at 27° S and at 0.86 $R_\odot$ in the QBO timescale (Figures 6(e) and (f)).

We then calculate the CCMs for each pair of flow and magnetic field data at each depth ranging from 0.71 $R_\odot$ and 1.00 $R_\odot$, and from 65° N to 65° S. We plotted the direction of causal influences found for the Schwabe and the QBO timescales to study whether there is a different pattern in causal relationship in different timescales (Figure 7).

In the Shcwabe timescale, the causal influence of the magnetic field on the flow field is stronger and is confined between the latitudes of ∼30° N and S generally at all depths, except for the shallow region reaching down to 0.85 $R_\odot$ and between ∼15° N and ∼10° S latitude. In this region, the causal influence of the flow field on the magnetic field is stronger (Figure 4(a)). Another important feature is above ∼45° N and S latitude; the direction of the causal influence switches generally to be from the flow field to the magnetic field with regions of bidirectional and reversed relationships observed in the southern and northern hemispheres, respectively. An interesting feature is seen between ∼45° and ∼60° N latitude and between ∼0.75 $R_\odot$ and ∼0.85 $R_\odot$, where the causal effects of the magnetic field on the flow field are stronger. A similar pattern also exists for the southern hemisphere; however, the degree of influence between the magnetic and flow fields in this region is very similar (Figure 4(a)).

The direction of the stronger causal effect in the QBO timescale, on the other hand, is mostly from the magnetic field to the flow field, at all latitudes and depths, with some small regions, especially below ∼0.85 $R_\odot$, showing the opposite behavior (Figure 7(b)). More specifically, in the latitudes between 0 and ∼30° S, the direction of stronger causal effect is more from the flow field to the magnetic field, while the same latitudinal band in the northern solar hemisphere shows that the effect of the magnetic field on the flow field is stronger (Figure 7(b)). Above ∼30° N and S latitude, the influence of the magnetic field on the flow field is stronger everywhere (Figure 7(b)).

4. Discussion and Conclusions

The results point out that the rotation rate residuals and average unsigned magnetic field strengths show different patterns in two different timescales. The strong unsigned magnetic field is confined in a band between ∼5° and ∼30° in the northern and southern hemispheres, where they show equator-ward propagation in the Schwabe timescale. In the QBO timescale, on the other hand, the magnetic field strengths fluctuate around the mean value, creating lower-than-average and higher-than-average magnetic field bands, which show both equator-ward and poleward propagation. These results are in line with Vecchio et al. (2012), who showed that there are poleward and equator-ward propagation bands in the radial and meridional components of the magnetic fields in the QBO timescales during solar cycles 21 and 22. The explanation for the differences in behavior observed in the unsigned magnetic fields comes from the generation of the toroidal magnetic fields by the solar dynamo. In the Schwabe timescales, this behavior is closely related to the emergence of the active regions, while in the QBO timescale, it resembles the pole- and equator-ward transportation of the residual magnetic field via flows after the bipolar active region cancels itself out (Vecchio et al. 2012). The amplitudes of variations in the Schwabe and the QBO timescales are very similar, having higher amplitudes confined between ∼5° and ∼30° in the northern and southern hemispheres with the maximum amplitudes around ∼20° N and S.

The rotation rate residuals in the Schwabe timescale exhibited faster-than-average and slower-than-average flow bands that form at ∼45° and propagate equator- and poleward. The slower-than-average flow bands generally coincide with regions where the magnetic field is stronger. This is a result of the back-reaction of the Lorentz Force on the flow field. We also observe a tail-like structure in the slower-than-average flow band, extending into the next cycle by around 2 yr at depths above ∼0.95 $R_\odot$. The tail-like structure, indicating the overlapping period between two consecutive cycles in the flow field, can be explained by flux transport dynamos with the Babcock–Leighton (BL) mechanism together with a turbulent α-effect operating throughout the convection zone. These are the main source for the generation of the poloidal field from a preexisting toroidal field (Passos et al. 2014; Simoniello et al. 2016). Solar dynamos that use only the BL mechanism and thin-shell dynamos with a turbulent α-effect, on the other hand, tend to generate longer overlapping periods between cycles (Dikpati & Gilman 2001; Dikpati et al. 2005; Bushby 2006; Karak & Miesch 2017; Inceoglu et al. 2017, 2019). An interesting feature that can be observed is the absence of this behavior at depths below ∼0.95 $R_\odot$.

The flow fields in the QBO timescale drew a very different picture with flow patterns distributed over all latitudes. The amplitudes of the slower-than-average and faster-than average flows increase with increasing depth. Additionally, the flow patterns in the QBO timescale, similar to those in the Schwabe timescale, change as we go deeper in the solar convection zone. At the depth of 0.99 $R_\odot$, the flow pattern in the QBO timescale closely resembles that in the Schwabe timescale, forming around ∼45° and propagating equator- and poleward. The deeper layers, on the other hand, exhibit different patterns than those in their Schwabe timescale counterparts.

The amplitude of variations in the Schwabe timescales depends mainly on latitude. Above ∼30° latitude, the amplitude increases with increasing latitudes, reaching its maximum above ∼55° latitude. Radially, the amplitudes do not exhibit big variations down to the depth of ∼0.78 $R_\odot$, below which the amplitudes get smaller with increasing depth. Below ∼30° latitude, the amplitudes of variations are almost the same at every latitude with a slight decrease with increasing depth. The amplitude of variations in the QBO, on the contrary, shows primarily radial dependence down to ∼0.78 $R_\odot$, where the amplitude increases with increasing depth, which also was previously observed for solar cycles 23 and 24, separately (Inceoglu et al. 2021). Different from the Schwabe timescale, the maximum amplitude is observed above ∼55° and below ∼0.78 $R_\odot$, where the amplitudes decrease with decreasing latitude. Considering that the slower-than-average flow band coincides with higher magnetic field regions, as a result of the back-reaction of the magnetic field on the flow field, one can argue that in the Schwabe timescale, the magnetic field is still mainly confined between ∼30° N and S latitude with similar amplitudes.

To investigate the interaction between the flow and magnetic fields, we assumed that the rotation profiles are symmetric and the magnetic field measured on the surface is nonlocal. It must

be noted that some asymmetries in the flow fields have been shown during the declining phase of cycle 23 and rising phase of solar cycle 24 at $\sim$0.99 $R_\odot$ using local helioseismological inversions (Lekshmi et al. 2018). However, our aim is to have an average picture of the interactions between the magnetic and flow fields.

Results from cross-correlation analyses, which measure the direction and the strength of the linear relationship at a time lag in the Schwabe timescale, show that latitudes between $\sim$30° latitude in N and S and below $\sim$0.95 $R_\odot$ show negative correlations. In this region, the magnetic field leads the flow field. This result is also supported by that from the CCM analyses, showing that the nonlinear causal influence is stronger from the magnetic field to the flow field. Above $\sim$0.95 $R_\odot$ and between $\sim$30° latitude in N and S latitudes, however, results from both the cross-correlation and the CCM analyses indicate that there is a positive correlation between the magnetic and flow fields, where the flow field leads the magnetic field, and the causal influence of the flow field on the magnetic field is stronger. This region is also where the turbulent α-effect is thought to be concentrated to generate the observed patterns in active region emergences during a solar cycle (Charbonneau 2020).

Above $\sim$35° latitude in N and S, there is a positive correlation between the flow and magnetic fields with a gradual transition from the magnetic field leading the flow field to the flow field leading the magnetic field with increasing latitude. The only exception for this pattern is in the high latitudes in the southern hemisphere, where the magnetic field leads the flow field. The positive correlations are also found to be stronger in the southern hemisphere. An interesting feature is that regions with strong linear positive correlations ($\rho > 0.75$) coincide with regions where the causal influence of the flow field on the magnetic field is stronger or almost equal. Another interesting feature is the region confined in the northern hemisphere between $\sim$45° and $\sim$55° and between $\sim$0.75 $R_\odot$ and $\sim$0.82 $R_\odot$, where the causal influence of the magnetic field on the flow field is stronger.

In the QBO timescale, on the other hand, the cross-correlation analyses do not exhibit a clear pattern. The negative and positive correlation patches, as well as the lead-lag relationship, are distributed all over different latitudes and depths. A similar, chaotic pattern can also be observed in the causal relationship between the magnetic and flow fields. There are more regions where the causal influence of the flow field on the magnetic field is stronger between $\sim$30° latitude in N and S at depths below $\sim$0.95 $R_\odot$, while above $\sim$30° latitude in N and S at all depths, the regions where the causal influence of the magnetic field on the flow field is stronger are more common.

One of the possible explanations for the double cycles is having a secondary dynamo operating in the subsurface region where the strong radial or latitudinal shear exists, while the primary dynamo operates at the bottom of the convection zone where a large-scale radial shear takes place (Benevolenskaya 1998). The physical mechanism that produces the high-frequency component is the helicity from the emerged magnetic field of the low-frequency component being imposed on the regions that generates the high-frequency component. Furthermore, the feedback of the low-frequency component on imposed helicity and the amplitude of the high-frequency component show a negative correlation, meaning that the double cycles can be achieved if the two magnetic field sources are weakly interacting. However, it must be noted that this is a simple model that uses only latitudinal shear where Cartesian coordinates are employed, and the results are therefore qualitative (Benevolenskaya 1998).

Käpylä et al. (2016) used a solar-like semi-global direct numerical simulation (DNS) of convection-driven dynamos and showed that the dominant mode exhibiting the most energy was around 0.85 $R_\odot$. This mode is accompanied by high-and low-frequency components, which operate near the surface around 0.98 $R_\odot$ and in the bottom of the convection zone near 0.72 $R_\odot$ (Käpylä et al. 2016). In addition, results from global 3D nonlinear turbulent MHD simulations, where the feedback of the Lorentz force on the large-scale differential rotation sets the cycle-length, showed that there can be two cycles that are nonlinearly coupled in the convection zone (Strugarek et al. 2018). Furthermore, these cycles can display different trends and dependencies, and result from different dynamos. The authors also showed that in their simulations they identified primary cycles from near $\sim$0.72 $R_\odot$ and secondary cycles originating from the $\sim$0.98 $R_\odot$ of the convective envelop of their model (Strugarek et al. 2018).

Using Sun-as-a-star Doppler velocity observations, Fletcher et al. (2010) suggested that the high-frequency component (the QBOs) is an additive contribution to the low-frequency component (the Schwabe cycles), and the amplitude envelope of it is governed by the Schwabe cycle. They also suggested that as the amplitudes of the QBOs seem to be independent of the frequency modes, pointing to a source region deeper than that of the Schwabe cycles (Fletcher et al. 2010), however, still within the upper 5% of the solar radius.

Another explanation for the QBOs comes from the TNOs resulting from the interplay between magnetic Rossby waves and differential rotation in the tachocline, leading the toroidal magnetic field to rise buoyantly in the convection zone (Dikpati et al. 2017, 2018). It must be noted that for this interaction to occur, the solar dynamo does not necessarily operate in the tachocline and can be distributed throughout the convection zone (Dikpati et al. 2018). The physical mechanism that generates the TNOs is the energy exchange between the magnetic Rossby waves and the differential rotation at the solar tachocline. More precisely, magnetic Rossby waves grow and increase their energy by stealing kinetic energy from the differential rotation through Reynolds stress; when the mean shear flow in the tachocline is unstable, this in turn results in the mean flow being tilted against the shear flow. When Rossby waves reach their maximum kinetic energy, they become weaker as the shear flow cannot provide more energy to the waves, and hence the Rossby waves give back kinetic energy to the mean flow and get tilted with the differential rotation (Dikpati et al. 2017, 2018). During the former phase of this oscillatory behavior, the top layers of the tachocline become deformed, creating bulges and depressions, where the tachocline toroidal field starts its buoyant rise in the solar convection zone and forms active regions on the solar surface (Dikpati et al. 2017, 2018).

Inceoglu et al. (2021) showed that the QBOs are present in the rotation rate residuals at target depths of 0.99 $R_\odot$, 0.95 $R_\odot$, and 0.90 $R_\odot$, indicating that the source region for the QBOs might extend into the deeper layers of the convection zone, and may not be confined to the upper 5% of the solar radius. We also showed here that the amplitude of variations in the rotation rate residuals in the QBO timescale increases with increasing

depth down to 0.78 $R_{\odot}$, after which the amplitude shows latitudinal dependency. This means that the amplitude of variations in the QBO timescale increases with increasing latitudes. Our results are more in line with the TNOs as source mechanisms for the QBOs, where higher-amplitude variations in the rotation rate residuals as we go deeper into the convection zone are expected.

The results from the cross correlations and CCMs also suggest that the interaction between the rotation rate residuals and magnetic field is not confined to a certain layer in the convective envelope, and it is rather distributed with no discernible pattern. For the Schwabe cycle, on the other hand, the source region is distributed across the convection zone, and it is confined between $\sim 30^{\circ}$ latitude in N and S, which are in line with those from the DNS and global 3D simulations. However, we must emphasize that the results from the cross-correlation and CCM analyses must be interpreted with caution because of the assumptions we had to make.

In conclusion, under the assumption that the flow fields are symmetric around the equator and the surface averaged unsigned magnetic field is nonlocal, the results from our analyses of the interaction between the rotation rate residuals and average unsigned magnetic field strengths in the Schwabe and QBO timescales suggest that the QBOs and Schwabe cycles originate from a global dynamo mechanism distributed throughout the convection zone. Thus, TNOs provide the more likely explanation for the generation of QBOs.

The authors acknowledge computing support from the National Solar Observatory. R.H. acknowledges support from STFC grant ST/V000500/1. SOHO is a project of international cooperation between ESA and NASA. HMI data are a courtesy of NASA/SDO and the HMI science team. This work was partially funded as part of the GOES-R Series NASA-NOAA program under the University of Colorado CIRES-NOAA cooperative agreement. The views, opinions, and findings contained in this report are those of the authors and should not be construed as an official National Oceanic and Atmospheric Administration, National Aeronautics and Space Administration, or other U.S. Government position, policy, or decision.

ORCID iDs

Fadil Inceoglu https://orcid.org/0000-0003-4726-3994
Rachel Howe https://orcid.org/0000-0002-3834-8585

References

Bazilevskaya, G., Broomhall, A. M., Elsworth, Y., & Nakariakov, V. M. 2014, SSRv, 186, 359
Benevolenskaya, E. E. 1998, ApJL, 509, L49
Berdyugina, S. V., & Usoskin, I. G. 2003, A&A, 405, 1121
Bushby, P. J. 2006, MNRAS, 371, 772
Charbonneau, P. 2020, LRSP, 17, 4
Dikpati, M., Cally, P. S., McIntosh, S. W., & Heifetz, E. 2017, NatSR, 7, 14750
Dikpati, M., & Gilman, P. A. 2001, ApJ, 559, 428
Dikpati, M., McIntosh, S. W., Bothun, G., et al. 2018, ApJ, 853, 144
Dikpati, M., Rempel, M., Gilman, P. A., & MacGregor, K. B. 2005, A&A, 437, 699
Fletcher, S. T., Broomhall, A.-M., Salabert, D., et al. 2010, ApJL, 718, L19
Gleissberg, W. 1939, Obs, 62, 158
Gurgenashvili, E., Zaqarashvili, T. V., Kukhianidze, V., et al. 2017, ApJ, 845, 137
Howe, R. 2009, LRSP, 6, 1
Howe, R., Christensen-Dalsgaard, J., Hill, F., et al. 2013, ApJL, 767, L20
Inceoglu, F., Arlt, R., & Rempel, M. 2017, ApJ, 848, 93
Inceoglu, F., Howe, R., & Loto'aniu, P. T. M. 2021, ApJ, 920, 49
Inceoglu, F., Simoniello, R., Arlt, R., & Rempel, M. 2019, A&A, 625, A117
Käpylä, M. J., Käpylä, P. J., Olspert, N., et al. 2016, A&A, 589, A56
Karak, B. B., & Miesch, M. 2017, ApJ, 847, 69
Kudela, K., Mavromichalaki, H., Papaioannou, A., & Gerontidou, M. 2010, SoPh, 266, 173
Lekshmi, B., Nandy, D., & Antia, H. M. 2018, ApJ, 861, 121
Liu, Y., Hoeksema, J. T., Scherrer, P. H., et al. 2012, SoPh, 279, 295
Passos, D., Nandy, D., Hazra, S., & Lopes, I. 2014, A&A, 563, A18
Rieger, E., Share, G. H., Forrest, D. J., et al. 1984, Natur, 312, 623
Roberts, J., & Roberts, T. D. 1978, JGR, 83, 5510
Scherrer, P. H., Bogart, R. S., Bush, R. I., et al. 1995, SoPh, 162, 129
Scherrer, P. H., Schou, J., Bush, R. I., et al. 2012, SoPh, 275, 207
Schwabe, H. 1844, AN, 21, 233
Simoniello, R., Finsterle, W., Salabert, D., et al. 2012, A&A, 539, A135
Simoniello, R., Jain, K., Tripathy, S. C., et al. 2013, ApJ, 765, 100
Simoniello, R., Tripathy, S. C., Jain, K., & Hill, F. 2016, ApJ, 828, 41
Strugarek, A., Beaudoin, P., Charbonneau, P., & Brun, A. S. 2018, ApJ, 863, 35
Suess, H. E. 1980, Radiocarbon, 22, 200
Sugihara, G., May, R., Ye, H., et al. 2012, Sci, 338, 496
Vecchio, A., Laurenza, M., Meduri, D., Carbone, V., & Storini, M. 2012, ApJ, 749, 27
Ye, H., & Sugihara, G. 2016, Sci, 353, 922
Zaqarashvili, T. V., Carbonell, M., Oliver, R., & Ballester, J. L. 2010, ApJL, 724, L95